

RESEARCH ARTICLE

[View Article Online](#)  
[View Journal](#) | [View Issue](#)



Cite this: *Inorg. Chem. Front.*, 2023, **10**, 3273

## A new 0D–2D $\text{CsPbBr}_3$ – $\text{Co}_3\text{O}_4$ heterostructure photocatalyst with efficient charge separation for photocatalytic $\text{CO}_2$ reduction†

Xin Zhong,‡<sup>a</sup> Xinmeng Liang,‡<sup>a</sup> Xinyu Lin,<sup>a</sup> Jin Wang, <sup>a,b</sup> Malik Zeeshan Shahid <sup>a</sup> and Zhengquan Li <sup>a,b</sup>

The effective spatial separation of photogenerated charge carriers is essential for realizing efficient  $\text{CO}_2$  conversion. Herein, a new  $\text{CsPbBr}_3$ – $\text{Co}_3\text{O}_4$  heterostructure photocatalyst was rationally developed for photocatalytic  $\text{CO}_2$  reduction. A facile synthetic strategy based on electrostatic interactions was utilized. The results revealed that the  $\text{CsPbBr}_3$ – $\text{Co}_3\text{O}_4$  hybrid exhibited a boosted evolution rate of  $64.6 \mu\text{mol g}^{-1} \text{h}^{-1}$  ( $\text{CO}$ :  $35.40 \mu\text{mol g}^{-1} \text{h}^{-1}$ ;  $\text{CH}_4$ :  $29.2 \mu\text{mol g}^{-1} \text{h}^{-1}$ ) with an electron consumption rate ( $R_{\text{electron}}$ ) of  $304.4 \mu\text{mol g}^{-1} \text{h}^{-1}$ , surpassing pristine  $\text{CsPbBr}_3$  or  $\text{Co}_3\text{O}_4$ . The high activity mainly arises from efficient charge separation and the directional transfer of electrons from  $\text{CsPbBr}_3$  to  $\text{Co}_3\text{O}_4$  *via* an intimately coupled heterointerface. Notably, the surface features (derived from the unique morphology) expedited the  $\text{CO}_2$  adsorption and accumulation of electrons at the  $\text{Co}_3\text{O}_4$  site which ultimately facilitated the conversion of  $\text{CO}_2$  over the  $\text{CsPbBr}_3$ – $\text{Co}_3\text{O}_4$  composite. This approach provides a strategy to design and modulate highly active metal oxide and perovskite-based photocatalysts and presents great potential for constructing a heterointerface for  $\text{CO}_2$  reduction.

Received 21st March 2023,  
Accepted 17th April 2023

DOI: 10.1039/d3qi00527e  
[rsc.li/frontiers-inorganic](http://rsc.li/frontiers-inorganic)

## 1. Introduction

The daily consumption of fossil fuels results in the emission of  $\text{CO}_2$ , causing universal environmental and energy issues.<sup>1–4</sup> Fixation of  $\text{CO}_2$  into value-added products such as  $\text{CO}$ ,  $\text{CH}_4$ ,  $\text{HCOOH}$ ,  $\text{CH}_3\text{OH}$ , *etc.* *via* solar-driven catalysis, also known as artificial photosynthesis, is a clean and sustainable solution.<sup>5–7</sup> However, it is challenging and suffers low conversion efficiency due to the high thermodynamic stability of  $\text{CO}_2$  molecules and the need for multi-electron transfer.<sup>8,9</sup> Recently, instead of using single-component photocatalysts, research efforts have been diverted to designing their low-cost heterostructures. Many materials, such as  $\text{C}_3\text{N}_4$ ,<sup>10,11</sup>  $\text{ZrO}_2$ ,<sup>12</sup>  $\text{TiO}_2$ ,<sup>13</sup>  $\text{Ta}_2\text{O}_5$ ,<sup>14</sup>  $\text{Nb}_2\text{O}_5$ ,<sup>15</sup> metal sulfides,<sup>16</sup> metal–organic frameworks,<sup>17</sup> metal complexes,<sup>7</sup> single-atom catalysts,<sup>18</sup>

MXenes,<sup>19</sup> conducting polymers,<sup>20</sup> metal halide perovskites,<sup>6,21</sup> *etc.*, have been reported aiming at activity enhancement *via* optimizing the light-harvesting and charge carrier kinetics. However, the search for a more effective candidate photocatalyst has not stopped.

Among numerous materials, all inorganic metal halide perovskites, particularly cesium lead-bromide perovskite quantum dots ( $\text{CsPbBr}_3$  QDs), are extremely competitive photocatalysts for  $\text{CO}_2$  reduction.<sup>1,6,22,23</sup> This is owing to their suitable energy band structure, small size, defect tolerance, and large carrier mobility as compared to other inorganic metal halide family members, *e.g.*  $\text{CsPbCl}_3$  and  $\text{CsPbI}_3$ .<sup>1,6,24–43</sup> However, pristine  $\text{CsPbBr}_3$  QDs suffer from instability and rapid recombination of electron–hole ( $e^-$ – $h^+$ ) pairs, leading to low activity. To address this issue, Xu *et al.* first utilized the  $\text{CsPbBr}_3$  QDs/graphene composite for the photocatalytic reduction of  $\text{CO}_2$ .<sup>43</sup> After that, several efforts were devoted to enhance its performance. For instance, our group designed  $\text{CsPbBr}_3$  QDs/ $\text{Bi}_2\text{WO}_6$ <sup>38</sup> and  $\text{CsPbBr}_3$  QDs coupled with covalent triazine frameworks,<sup>36</sup> and both exhibited enhanced charge separation and led to improved  $\text{CO}_2$  photoreduction. But the produced gas was mainly  $\text{CO}$  and only a minimum of  $\text{CH}_4$  was detected. This was possibly due to the lack of sufficient accumulation of reductive electrons at catalytic sites.

<sup>a</sup>Key Laboratory of the Ministry of Education for Advanced Catalysis Materials, Zhejiang Normal University, Jinhua, Zhejiang 321004, P. R. China.

E-mail: [zqli@zjnu.edu.cn](mailto:zqli@zjnu.edu.cn), [zeeshan-nano@zjnu.edu.cn](mailto:zeeshan-nano@zjnu.edu.cn), [wangjin@zjnu.edu.cn](mailto:wangjin@zjnu.edu.cn)

<sup>b</sup>Zhejiang Institute of Optoelectronics, Zhejiang Normal University, Jinhua, Zhejiang 321004, P. R. China

† Electronic supplementary information (ESI) available. See DOI: <https://doi.org/10.1039/d3qi00527e>

‡ These authors contributed equally.

So, we further our research to find some suitable materials which can form an intimately coupled interface with  $\text{CsPbBr}_3$  QDs and enable efficient photocatalysis to generate both  $\text{CO}$  and  $\text{CH}_4$ , thereby overcoming the intrinsic issues of  $\text{CsPbBr}_3$  QDs.

We found that the transition metal oxide photocatalyst cobalt oxide ( $\text{Co}_3\text{O}_4$ ) is an ideal non-precious catalyst for  $\text{CO}_2$  reduction as it exhibits suitable band alignment, efficient charge-carrier flux capability, and chemical/thermodynamic stability.<sup>44–52</sup> However, the typical single component  $\text{Co}_3\text{O}_4$  may suffer limited preservation of reductive electrons as well as hindered spatial separation of  $e^-$ – $h^+$  pairs. Multiple morphologies have been constructed to meet such limitations, such as nanorods,<sup>53</sup> ultrathin nanosheets,<sup>54</sup> nanofibers,<sup>55</sup> hollow dodecahedra,<sup>48</sup> porous structures,<sup>56</sup> and mesoporous two-dimensional (2D) hexagonal nanoplatelets (HPs) with various facets and catalytically active sites.<sup>45,57</sup> For example, Gao *et al.* first developed [112] facet-rich  $\text{Co}_3\text{O}_4$  HPs,<sup>52</sup> and then later on Zhu *et al.* constructed the  $\text{Co}_3\text{O}_4/\text{g-C}_3\text{N}_4$  (2D/2D) hybrid,<sup>57</sup> both intended to facilitate the separation of charge carriers for photocatalytic  $\text{CO}_2$  conversion. Inspiringly, we intend to develop a high-performance  $\text{Co}_3\text{O}_4$  heterostructure catalyst by simultaneously promoting charge separation and preserving the reductive electrons. It is widely accepted that constructing a heterostructure is efficient for channelizing and accelerating the separation and transfer of  $e^-$ – $h^+$  pairs *via* a strongly coupled interface developed through proper band alignment and work functions ( $\phi$ ).<sup>47,58–61</sup> Therefore, constructing a hybrid between  $\text{CsPbBr}_3$  QDs and  $\text{Co}_3\text{O}_4$  HPs probably can result in an improved photocatalytic performance toward  $\text{CO}_2$  reduction. To the best of our knowledge, there is no report on the fabrication of  $\text{CsPbBr}_3$  QDs on  $\text{Co}_3\text{O}_4$  HPs, and it is desirable to design and construct a new heterostructure based on  $\text{CsPbBr}_3$  QDs and  $\text{Co}_3\text{O}_4$  HPs for  $\text{CO}_2$  photoreduction.

Herein, a  $\text{CsPbBr}_3$ – $\text{Co}_3\text{O}_4$  heterojunction photocatalyst is developed *via* electrostatic self-assembly between  $\text{Co}_3\text{O}_4$  HPs and  $\text{CsPbBr}_3$  QDs for photocatalytic  $\text{CO}_2$  reduction. Investigations confirmed the successful formation of the  $\text{CsPbBr}_3$ – $\text{Co}_3\text{O}_4$  hybrid. Diverse physicochemical and optoelectronic characterization studies revealed that: (i)  $\text{Co}_3\text{O}_4$  HPs acted as a supporting matrix to collect electrons from  $\text{CsPbBr}_3$ , rendering electron localization; (ii) the  $\text{CsPbBr}_3$ – $\text{Co}_3\text{O}_4$  hybrid exhibited compact heterointerfaces, facilitating robust charge separation with hampered  $e^-$ – $h^+$  pair recombination; (iii) the  $\text{Co}_3\text{O}_4$  side offers numerous mesopores and catalytic sites, which facilitate the better capturing and activation of  $\text{CO}_2$  molecules. Consequently,  $\text{CsPbBr}_3$ – $\text{Co}_3\text{O}_4$  showed improved activity for the generation of  $\text{CO}$  and  $\text{CH}_4$ , with an evolving rate of 35.40 and 29.2  $\mu\text{mol g}^{-1} \text{h}^{-1}$ , respectively, surpassing their pristine counterparts *i.e.*,  $\text{CsPbBr}_3$  QDs and  $\text{Co}_3\text{O}_4$  HPs, as well as recent state-of-the-art photocatalysts (Table S1†). This work highlights the rational design of new metal halide perovskite-based photocatalysts and addresses the critical issues regarding charge carrier kinetics to realize efficient solar-driven  $\text{CO}_2$  conversion.

## 2. Experimental section

### 2.1. Synthesis of $\text{CsPbBr}_3$ QDs

To obtain  $\text{CsPbBr}_3$  QDs, the reported method was followed (see also in Fig. S1†).<sup>62</sup> Briefly, for the Cs-OA stock solution, 0.2 g of cesium carbonate ( $\text{Cs}_2\text{CO}_3$ ), 10 mL of octadecene (ODE,  $\text{C}_{18}\text{H}_{36}$ ), and 0.6 mL of oleic acid (OA,  $\text{C}_{18}\text{H}_{34}\text{O}_2$ ) were loaded into a three-necked round bottom flask. Under Ar flow, the temperature was increased to 120 °C and a clear light-yellow solution was obtained. The temperature was increased to 150 °C just before the hot injection. For the Pb stock solution, 0.1380 g of lead bromide ( $\text{PbBr}_2$ ) and 10 mL of ODE were added into a 50 mL three-necked round bottom flask, under Ar flow, the temperature was increased to 120 °C to get a white turbid liquid and maintained it for 30 min. Next, the temperature was further increased to 165 °C, and 1.5 mL OA and 1.1 mL OAm were added to the Pb stocks. When a yellow homogeneous solution was obtained, 0.8 mL of the Cs-stock solution was swiftly injected into it. After 5 s, the mixture was immediately cooled down using an ice-water bath. The original solution was directly centrifuged at 8000 rpm for 5 min and further washed with ethyl acetate and isopropanol to remove the organic residue. Finally, the  $\text{CsPbBr}_3$  QDs collected and stored in *n*-hexane are added in an equal volume.

### 2.2. Preparation of $\text{Co}_3\text{O}_4$ HPs

To obtain  $\text{Co}_3\text{O}_4$  HPs, the previously reported method was modified (see also in Fig. S2†).<sup>52</sup> Firstly,  $\beta$ - $\text{Co}(\text{OH})_2$  precipitates were prepared. 0.2379 g (5 mmol) of cobalt chloride hexahydrate ( $\text{CoCl}_2 \cdot 6\text{H}_2\text{O}$ ), 1.6823 g (60 mmol) of cyclohexamethylenetetramine (urotropine), 180 mL of deionized water and 20 mL of ethanol were added into a beaker under stirring. The mixture was heated in an oil bath to 90 °C for 1 h to obtain a pink solution. After cooling it to an ambient temperature, it was centrifuged at 9000 rpm for 15 min to obtain a pink precipitate of  $\beta$ - $\text{Co}(\text{OH})_2$ . Subsequently, 50 mL of deionized water and 50 mL of ethanol were added, and the  $\beta$ - $\text{Co}(\text{OH})_2$  precipitate was redispersed by ultrasonication. The sample was collected by centrifuging at 9000 rpm for 15 min. This operation was repeated 3 times. The obtained precipitate was freeze-dried under vacuum for 6 hours. Finally, the precipitate was transferred into a cuboid crucible and put into a muffle furnace for calcination at 400 °C for 3 h to obtain a black powder of  $\text{Co}_3\text{O}_4$  HPs.

### 2.3. Synthesis of the $\text{CsPbBr}_3$ – $\text{Co}_3\text{O}_4$ heterostructure

The  $\text{CsPbBr}_3$ – $\text{Co}_3\text{O}_4$  heterostructure was prepared using a solution-processed approach at room temperature. First, 0.5 mg of the  $\text{Co}_3\text{O}_4$  HP powder was dispersed into 250  $\mu\text{L}$  of ethanol under uninterrupted stirring. Second, 400  $\mu\text{L}$  (2 mg) of  $\text{CsPbBr}_3$  QDs were dispersed into 5 mL of ethyl acetate. Third, the  $\text{CsPbBr}_3$  QD solution was swiftly added into the solution of  $\text{Co}_3\text{O}_4$  HPs and mechanically stirred at room temperature in the dark for 30 min. Finally, the mixture was ultrasonicated for another 30 min under ambient conditions. The obtained solution was centrifuged at 8000 rpm for 5 min, and the precipitate

was vacuum dried overnight at 45 °C to obtain the  $\text{CsPbBr}_3$ – $\text{Co}_3\text{O}_4$  heterojunction. This synthesis was performed with an optimum mass ratio ( $\text{Co}_3\text{O}_4$  HPs :  $\text{CsPbBr}_3$  QDs) *i.e.*, 1 : 4, and a similar method was followed to obtain various mass ratios such as 1 : 1, 1 : 2, 1 : 8, and 1 : 16. Step by step addition of  $\text{Co}_3\text{O}_4$  HPs and  $\text{CsPbBr}_3$  QDs as well as the formation process of the  $\text{CsPbBr}_3$ – $\text{Co}_3\text{O}_4$  heterojunction are also picturized and described in Fig. S3.† The details of all materials and other characterization studies for physicochemical and optoelectronic properties are provided in the ESI.†

### 3. Results and discussion

#### 3.1. Illustration of the synthesis process and verification of the heterostructure formation

Firstly,  $\text{CsPbBr}_3$  QDs (0D) was precisely prepared *via* a typical hot-injection method (Fig. S1†).<sup>62</sup> Subsequently,  $\text{Co}_3\text{O}_4$  HPs (2D) holding rich facets [112] were synthesized through the calcination of brucite-like cobalt hydroxide  $\beta\text{-Co(OH)}_2$  precipitates (Fig. S2†).<sup>52</sup> Finally, to obtain a 0D/2D  $\text{CsPbBr}_3$ – $\text{Co}_3\text{O}_4$  heterojunction, their mixture at an optimum mass ratio 4 : 1 ( $\text{CsPbBr}_3$  QDs :  $\text{Co}_3\text{O}_4$  HPs) was exclusively stirred in a solution of ethyl acetate and ethanol at room temperature (Scheme 1, see details in Fig. S3†). The tactic used here is based on the Coulomb electrostatic assembly which enables the incorporation of  $\text{CsPbBr}_3$  QDs and  $\text{Co}_3\text{O}_4$  HPs. The zeta potentials of pristine  $\text{CsPbBr}_3$  QDs and  $\text{Co}_3\text{O}_4$  HPs are 4.80 mV and –3.10 mV, respectively (Fig. S4†), which indicates oppositely charged surfaces encounter electrostatic attractions, resulting in the formation of  $\text{CsPbBr}_3$ – $\text{Co}_3\text{O}_4$ . Such a kind of electrostatic self-assembly would possess a strong heterointerface, beneficial for interfacial charge transfer.<sup>63</sup>

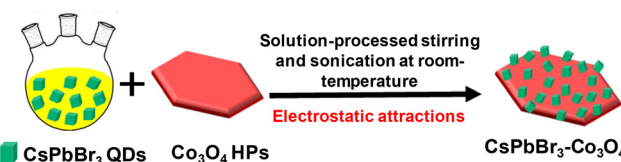
To confirm the successful formation of the  $\text{CsPbBr}_3$ – $\text{Co}_3\text{O}_4$  hybrid, powder X-ray diffraction (XRD) was first conducted (Fig. 1a). Pristine  $\text{CsPbBr}_3$  QDs exhibit a typical cubic-phase (JCPDS card, No. 75-0412). Meanwhile, pristine  $\text{Co}_3\text{O}_4$  HPs show diffraction patterns associated with the face-centred cubic phase of the spinel  $\text{Co}_3\text{O}_4$  (JCPDS card No. 74-1657). Notably, strong signals of all peaks emerged and co-existed in the  $\text{CsPbBr}_3$ – $\text{Co}_3\text{O}_4$  hybrid, illustrating the successful formation of the heterojunction and the crystal phases were well maintained. To confirm this claim, nitrogen adsorption–desorption analysis was performed (Table S2†). It can be seen that after the precise formation of the heterojunction, the pore size and pore volume were reduced from 31.3 nm to 21.21 nm

and 0.1325  $\text{cm}^3 \text{g}^{-1}$  to 0.0266  $\text{cm}^3 \text{g}^{-1}$  respectively. In addition, the BET surface area also decreased from 16.9  $\text{m}^2 \text{g}^{-1}$  to 5.016  $\text{m}^2 \text{g}^{-1}$ . This result indicates that the mesopores of  $\text{Co}_3\text{O}_4$  were occupied by  $\text{CsPbBr}_3$  QDs. Besides in the XRD, an exclusive color transformation was observed from black ( $\text{Co}_3\text{O}_4$ -HPs, Fig. 1b) and bright yellow ( $\text{CsPbBr}_3$  QDs, Fig. 1c) to dark grey ( $\text{CsPbBr}_3$ – $\text{Co}_3\text{O}_4$ , Fig. 1d). In addition, under ultraviolet irradiation, the  $\text{CsPbBr}_3$ – $\text{Co}_3\text{O}_4$  heterojunction demonstrated a dark green fluorescence in comparison with the bright green fluorescence of  $\text{CsPbBr}_3$  QDs (Fig. S5†). Such color transformations further endorse that the heterojunction was constructed successfully in a well-controlled manner *via* a current facile strategy.

Transmission electron microscopy (TEM) and scanning electron microscopy (SEM) analysis further confirmed the formation of the heterojunction.  $\text{CsPbBr}_3$  QDs exhibited an average size of about 12 nm (Fig. 1e and inset), whereas  $\text{Co}_3\text{O}_4$  exhibits a hexagonal platelet-like structure with lateral sizes of  $\sim 4 \pm 1 \mu\text{m}$ , and a thickness of about  $\sim 50 \pm 10 \text{ nm}$ , a dominant facet (112), and mesopores (Fig. 1f and inset). Importantly, after incorporating  $\text{CsPbBr}_3$  QDs into  $\text{Co}_3\text{O}_4$  HPs, several facts were noticed. (i) Both  $\text{CsPbBr}_3$  QDs and  $\text{Co}_3\text{O}_4$  HPs co-existed with well-defined morphologies, and their sizes were preserved without any further ripening, verifying that the synthesis was well-controlled (Fig. 1g). (ii) Besides electrostatic interactions, the huge surface energy of  $\text{CsPbBr}_3$  QDs could drive its face-to-face attaching to  $\text{Co}_3\text{O}_4$  HPs. (iii)  $\text{CsPbBr}_3$  QDs were well dispersed (denoted by yellow circles) all over  $\text{Co}_3\text{O}_4$  HPs, both on the inner side (Fig. 1g and inset) and on the boundary sides (Fig. 1h) and this would facilitate the formation of a rich heterointerface. (iv) Even though most of the mesopores were occupied by  $\text{CsPbBr}_3$  QDs, still many mesopores could be observed as denoted by the marked area in green (Fig. 1g, h, and the inset).

Such accessible mesopores are not only beneficial for supporting  $\text{CO}_2$  adsorption but also facilitate the exposure of the innermost lattice surfaces for the rapid transfer of photo-induced  $e^-$  to the outermost active surface sites.<sup>52,57</sup> More clear evidence regarding the formation of the heterointerface was collected *via* high-resolution TEM analysis (HRTEM, Fig. 1i and j). The spacing in the lattice fringes was found to match well with both constituents, that is, 0.58 nm and 0.285 nm being the corresponding planes of  $\text{CsPbBr}_3$  and  $\text{Co}_3\text{O}_4$  respectively (Fig. 1j). Accordingly, the HAADF and energy dispersive X-ray (EDX) mapping analysis depicts the precise incorporation and distribution of all elements including Cs, Pb, Br, Co, and O in the  $\text{CsPbBr}_3$ – $\text{Co}_3\text{O}_4$  heterojunction (Fig. 1k–p). The above results are in-line with the XRD and TEM analysis, validating the formation of the heterojunction with finely dispersed  $\text{CsPbBr}_3$  QDs on the support matrix of  $\text{Co}_3\text{O}_4$  HPs.

Next, surface chemical states and interfacial interaction in the  $\text{CsPbBr}_3$ – $\text{Co}_3\text{O}_4$  heterojunction were evaluated *via* high-resolution X-ray photoelectron spectroscopy (XPS) of Cs 3d, Pb 4f, Br 3d, Co 2p, and O 1s. It is noteworthy that, in comparison with  $\text{CsPbBr}_3$  QDs, the binding energy of Cs 3d (Fig. 2a), Pb 4f



**Scheme 1** Illustration for the formation of the  $\text{CsPbBr}_3$ – $\text{Co}_3\text{O}_4$  heterojunction *via* electrostatic attraction.

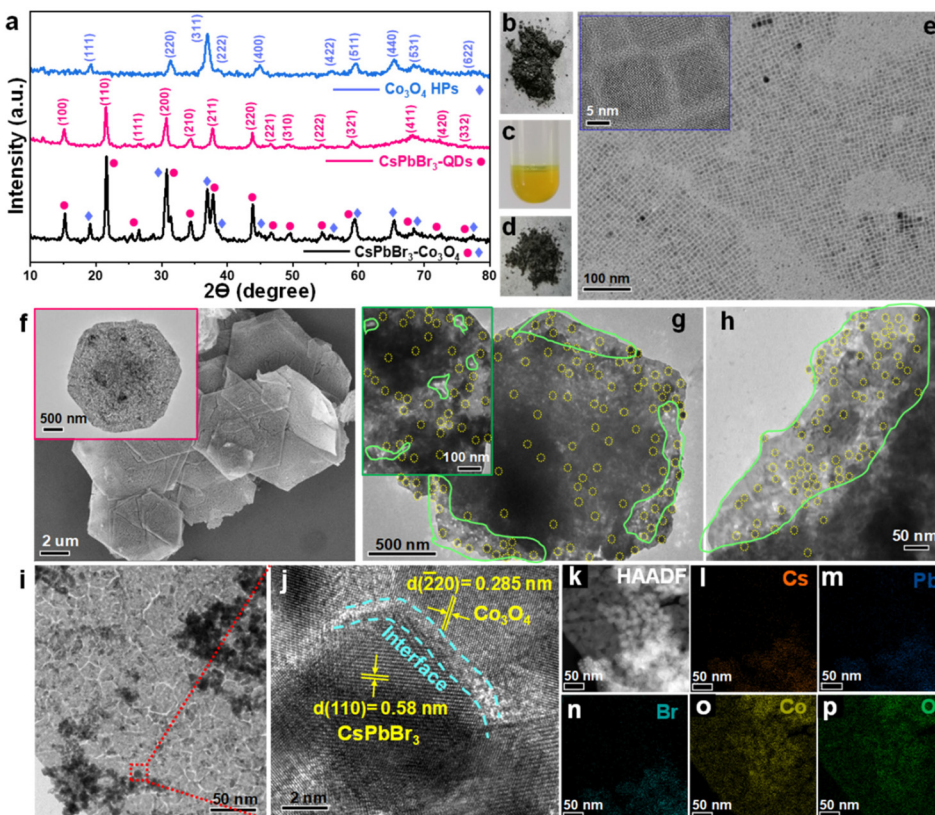


**Fig. 1** (a) Comparison of the XRD pattern for the as-prepared products within the 2 theta range  $10^\circ$ – $80^\circ$ , where pink circles and blue diamonds denote the corresponding peaks in the  $\text{Co}_3\text{O}_4$ – $\text{CsPbBr}_3$  heterojunction originating from pristine products. Exclusive color transformation of the as-synthesized products where (b)  $\text{Co}_3\text{O}_4$  HPs black, (c)  $\text{CsPbBr}_3$  QDs bright yellow, and (d)  $\text{CsPbBr}_3$ – $\text{Co}_3\text{O}_4$  dark grey. (e) The TEM image of pristine  $\text{CsPbBr}_3$  QDs and the corresponding inset with high magnification. (f) The SEM image with low magnification and the inset is the TEM image for a single particle of  $\text{Co}_3\text{O}_4$  HPs showing a hexagonal platelet-like morphology. (g) The TEM image of a  $\text{Co}_3\text{O}_4$ – $\text{CsPbBr}_3$  heterojunction and the corresponding inset which was captured from the central side of a random particle and (h) the image taken from the boundary side. Finely dispersed  $\text{CsPbBr}_3$  QDs are denoted with yellow circles and the pores are denoted with green marked areas. (i) and (j) HRTEM images, and (k–p) HAADF and EDX mapping results for the  $\text{Co}_3\text{O}_4$ – $\text{CsPbBr}_3$  heterojunction.

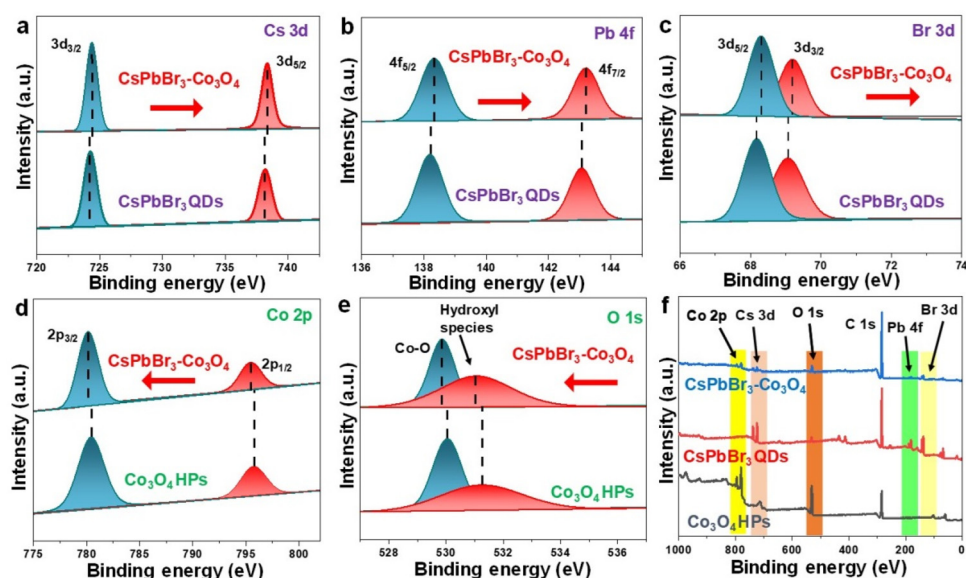


**Fig. 2** Comparative representation of high-resolution XPS spectra for (a) Cs 3d, (b) Pb 4f, (c) Br 3d, (d) Co 2p, and (e) O 1s in all the synthesized products. (f) The XPS survey spectrum highlights the co-existence of  $\text{CsPbBr}_3$  QDs and  $\text{Co}_3\text{O}_4$  HPs in the  $\text{CsPbBr}_3$ – $\text{Co}_3\text{O}_4$  heterojunction.

(Fig. 2b), and Br 3d (Fig. 2c) faced a positive shift in the heterojunction. This result strongly endorsed the close interfacial contact between QDs and HPs. Meanwhile, the XPS of Co 2p spectra signals were comparatively examined for  $\text{CsPbBr}_3$ – $\text{Co}_3\text{O}_4$  and  $\text{Co}_3\text{O}_4$  HPs (Fig. 2d), where two binding energy values at  $796 \pm 0.2$  eV and  $780 \pm 0.2$  eV fit to Co 2p<sub>1/2</sub> and Co 2p<sub>3/2</sub>, respectively, which normally attributed to two main regions *i.e.*,  $\text{Co}^{2+}$  and  $\text{Co}^{3+}$ .<sup>44</sup> As is known the theoretical value for the atomic ratio  $\text{Co}^{2+}/\text{Co}^{3+}$  is 0.5 (*i.e.*, perfect  $\text{Co}_3\text{O}_4$ ), but this value may increase in the presence of surface defects or oxygen vacancies (OVs).<sup>44</sup> Herein, no signal corresponding to defects in O 1s spectra (Fig. 2e) was found, which means that  $\text{Co}_3\text{O}_4$  synthesized here is perfect and in an equally balanced state. Notably, the absence of OVs also indicates that the high crystallinity of  $\text{Co}_3\text{O}_4$  was maintained after forming the  $\text{CsPbBr}_3$ – $\text{Co}_3\text{O}_4$  heterojunction. Meanwhile, a slight negative shift towards the lower binding energy was observed, demonstrating the interaction between  $\text{Co}_3\text{O}_4$  and  $\text{CsPbBr}_3$  (Fig. 2d). Moreover, relative O 1s spectra disclosed two main peaks that fit with the hydroxyl species and Co–O bond respectively. In addition, the obvious co-existence of  $\text{CsPbBr}_3$  QDs and  $\text{Co}_3\text{O}_4$  HPs is supported through the XPS survey spectrum (Fig. 2f). All the characteristic peaks are assigned to Cs, Pb, Br, Co, and O (highlighted with bars), affirming the formation of the  $\text{CsPbBr}_3$ – $\text{Co}_3\text{O}_4$  heterojunction.

### 3.2. Investigation of the photocatalytic activity for $\text{CO}_2$ reduction

The activity of the as-synthesized  $\text{CsPbBr}_3$ – $\text{Co}_3\text{O}_4$  heterojunction for  $\text{CO}_2$  photocatalytic reduction is evaluated under the solid–gas environment using 50  $\mu\text{L}$  of water as the proton source (see details in the ESI section 1.3†).<sup>36,38,63</sup> In particular, no sacrificial agent was used, and visible light was irradiated during photocatalysis. As shown in Fig. 3a, the pristine components only can produce limited CO and negligible  $\text{CH}_4$ , calculated to be 14.23 and 0.39 (for  $\text{CsPbBr}_3$  QDs) and 9.52 and 0.46 (for  $\text{Co}_3\text{O}_4$  HPs)  $\mu\text{mol g}^{-1} \text{h}^{-1}$ , respectively. Notably, the  $\text{CsPbBr}_3$ – $\text{Co}_3\text{O}_4$  heterojunction delivered an enhanced performance for the evolution of CO and  $\text{CH}_4$ , which is 35.40 and 29.2  $\mu\text{mol g}^{-1} \text{h}^{-1}$ , respectively. The corresponding electron consumption rate ( $R_{\text{electron}}$ , see the formula in Table S2†) was found to be 304.4  $\mu\text{mol g}^{-1} \text{h}^{-1}$ , which is 9.51 and 13.4 fold larger than that of pristine  $\text{CsPbBr}_3$  QDs and  $\text{Co}_3\text{O}_4$  HPs,

respectively. The maximum cumulative production of CO and  $\text{CH}_4$  after a 6-hour reaction was 211.58 and 175.31  $\mu\text{mol g}^{-1}$ , respectively (Fig. S6†). The current performance of the  $\text{CsPbBr}_3$ – $\text{Co}_3\text{O}_4$  heterojunction was found to be exceeding that of the pristine counter components as well as recent state-of-the-art photocatalysts (Table S1†). Moreover, altering the dosage ratio of  $\text{Co}_3\text{O}_4$  :  $\text{CsPbBr}_3$  in the heterojunction could greatly influence the activity, for instance, the upper limit of gases was only reached with an optimum mass ratio of 1 : 4 (Fig. S7†).

More and/or less dosage of  $\text{CsPbBr}_3$  than the optimum value in the heterojunction is not conducive to producing CO and  $\text{CH}_4$  in high yields, maybe due to the insufficient amount and/or blockage of active sites respectively, and this phenomenon was found to be consistent with the literature.<sup>38</sup> Additionally, control experiments were performed to confirm the origin of CO, and  $\text{CH}_4$  during photocatalysis (Fig. 3b). First, under an argon atmosphere, traces of CO or  $\text{CH}_4$  was found, which shows that feed-stock  $\text{CO}_2$  is necessary to run the photocatalytic reduction reaction.<sup>36,38,63</sup> Second, nothing was detected under the dark conditions, which again confirms light irradiation is required to obtain CO and  $\text{CH}_4$  from the reduction of  $\text{CO}_2$ . Finally, the optimum result could only be achieved using the  $\text{CsPbBr}_3$ – $\text{Co}_3\text{O}_4$  heterojunction with a mass ratio of 1 : 4 as the photocatalyst,  $\text{CO}_2$  gas as the feedstock, and solar light illumination ( $\lambda > 400$  nm). To further verify the origin of the carbon source of the photo-generated CO and  $\text{CH}_4$ ,  $^{13}\text{CO}_2$  isotope labelling was performed and the GC-MS result is displayed in Fig. S8.† Evidently, the signals belonging to  $^{13}\text{CO}$  ( $m/z$  29) and  $^{13}\text{CH}_4$  ( $m/z$  17) are derived from  $^{13}\text{CO}_2$ , validating that  $\text{CO}_2$  feedstock is the actual carbon source. Likewise, the oxidation of water to oxygen further validates the continuous supply of protons during  $\text{CO}_2$  conversion (Fig. S9†). Furthermore, the  $\text{CsPbBr}_3$ – $\text{Co}_3\text{O}_4$  heterojunction can remain stable during the consecutive 5 cycles (Fig. 3c). The morphological and structural characteristics of the  $\text{CsPbBr}_3$ – $\text{Co}_3\text{O}_4$  heterojunction are well-maintained after photocatalysis (Fig. S10a and S10b†).

### 3.3. Unveiling of the origins for improved activity

The origins of the possible enhanced activity were investigated and have been described systematically. The  $\text{CO}_2$  adsorption

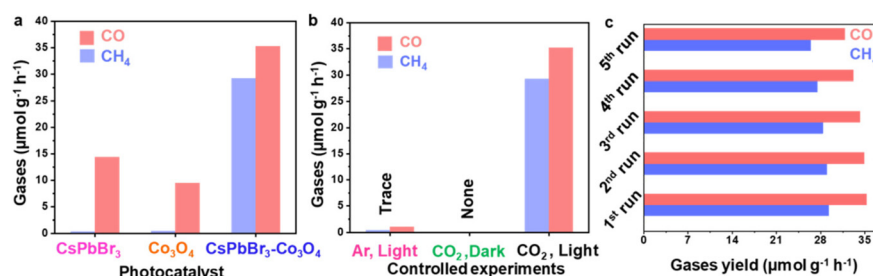


**Fig. 3** (a) A comparative depiction of the catalytic activity in terms of the produced gases CO and  $\text{CH}_4$  using the as-synthesized  $\text{CsPbBr}_3$  QDs,  $\text{Co}_3\text{O}_4$  HPs, and  $\text{CsPbBr}_3$ – $\text{Co}_3\text{O}_4$  heterojunction. (b) Controlled experiments were performed under different reaction conditions to produce CO and  $\text{CH}_4$  to examine the origin of the evolved gases. (c) Stability test of the  $\text{CsPbBr}_3$ – $\text{Co}_3\text{O}_4$  heterojunction for 5 consecutive cycles.

on the surface of the photocatalyst is a primary step that would further govern its activation and conversion. And it is well-known that  $\text{CsPbBr}_3$  QDs have a large surface area and are capable of adsorbing more  $\text{CO}_2$  on their surface.<sup>32,43</sup> As verified by the TEM analysis, the size of  $\text{CsPbBr}_3$  QDs remained unchanged after forming a hybrid with  $\text{Co}_3\text{O}_4$  HPs, indicating that it would exhibit similar  $\text{CO}_2$  adsorption activity on its surface. Likewise,  $\text{Co}_3\text{O}_4$  HPs also possess numerous adsorptions sites derived from their structural mesopores. Although most of the mesopores are occupied by  $\text{CsPbBr}_3$  QDs (Fig. S11 and Table S2†), additional porosities are still accessible in the heterojunction (as shown in the green marked area in Fig. 1g and h). These porosities would actively endure the  $\text{CO}_2$  adsorption.<sup>52,57</sup>

As the light absorption range is a key factor in solar-driven catalysis, to investigate the light-harvesting ability of the as-prepared components, diffuse reflectance spectra (DRS) were recorded. Both  $\text{CsPbBr}_3$  QDs and  $\text{Co}_3\text{O}_4$  HPs show a strong visible light response within the wavelength range of 400–600 nm, and their corresponding energy band gaps ( $E_g$ ), determined to be 2.36 eV and 2.31 eV, respectively, are well-consistent with the literature (Fig. 4a and b and corresponding insets).<sup>38,52</sup> Where;  $E_g$  is estimated through Tauc plots using the equation  $a\hbar\nu = A(\hbar\nu - E_g)^n$  (see details in section 1.5 of the ESI†). It is to be noted that  $E_{1g} = 1.83$  eV is attributed to the  $\text{O}^{2-} \rightarrow \text{Co}^{3+}$  excitation and is not a real energy bandgap of  $\text{Co}_3\text{O}_4$  HPs.<sup>52,64–66</sup> The enhanced light absorption ability of both components in the  $\text{CsPbBr}_3$ – $\text{Co}_3\text{O}_4$  heterojunction supports its higher catalytic activity. Moreover, the valence and conduction band positions ( $E_{\text{VB}}$  and  $E_{\text{CB}}$ ) strongly define the thermodynamic feasibility of  $\text{CO}_2$  reduction reactions. According to the reported results, the  $E_{\text{CB}}$  of  $\text{Co}_3\text{O}_4$  and  $\text{CsPbBr}_3$  are  $-0.64$  eV<sup>52</sup> and  $-0.99$  eV,<sup>36</sup> respectively, and cor-

respondingly, the calculated  $E_{\text{VB}}$  for  $\text{Co}_3\text{O}_4$  HPs and  $\text{CsPbBr}_3$  QDs are 1.67 eV and 1.37 eV, respectively. Hence, the consequent  $\text{CsPbBr}_3$ – $\text{Co}_3\text{O}_4$  heterojunction possess efficient light harvesting ability with staggered band alignment as depicted in Fig. 5a, further endorsing an uninterrupted  $\text{CO}_2$  conversion.

The rapid radiative recombination of photoinduced  $e^-h^+$  pairs in pristine  $\text{CsPbBr}_3$  QDs can lead to low  $\text{CO}_2$  conversion efficiency.<sup>24</sup> This was exclusively observed, where the intense photoluminescence (PL) spectra signal for pristine  $\text{CsPbBr}_3$  (Fig. 4c) confirmed its low catalytic activity. However, after immobilizing  $\text{CsPbBr}_3$  QDs on  $\text{Co}_3\text{O}_4$  HPs, the results dramatically changed towards low PL intensity, identifying the significantly hindered recombination of  $e^-h^+$  pairs over the  $\text{CsPbBr}_3$ – $\text{Co}_3\text{O}_4$  heterojunction (Fig. 4c and Fig. S12†). This finding matched well with the enhanced photocatalytic performance. This also means, combining such photocatalysts can substantially quench the radiative recombination of the metal halide perovskite, thereby exhibiting high activity. Likewise, to investigate the charge transfer kinetics, PL decay was also inquired *via* time-resolved photoluminescence spectroscopy (TRPL, curves were fitted with a bi-exponential function, Table S3† and Fig. 4d). The  $\text{CsPbBr}_3$ – $\text{Co}_3\text{O}_4$  heterojunction demonstrated a shorter lifetime ( $\tau_{\text{avg}} = 45.04$  ns) in comparison with pristine  $\text{CsPbBr}_3$  QDs ( $\tau_{\text{avg}} = 47.43$  ns). This outcome further verified the restrained recombination of  $e^-h^+$  pairs and their efficient separation in the  $\text{CsPbBr}_3$ – $\text{Co}_3\text{O}_4$  hybrid. Besides charge recombination, charge transfer kinetics and their directional transfer are decisive to realize an improved  $\text{CO}_2$  conversion.<sup>61,67,68</sup> Therefore, these were investigated for the  $\text{CsPbBr}_3$ – $\text{Co}_3\text{O}_4$  heterojunction through electrochemical impedance spectroscopy (EIS) and transient photocurrent responses (TPR). The smallest arc radius was seen for the  $\text{CsPbBr}_3$ – $\text{Co}_3\text{O}_4$  heterojunction followed by  $\text{CsPbBr}_3$  QDs

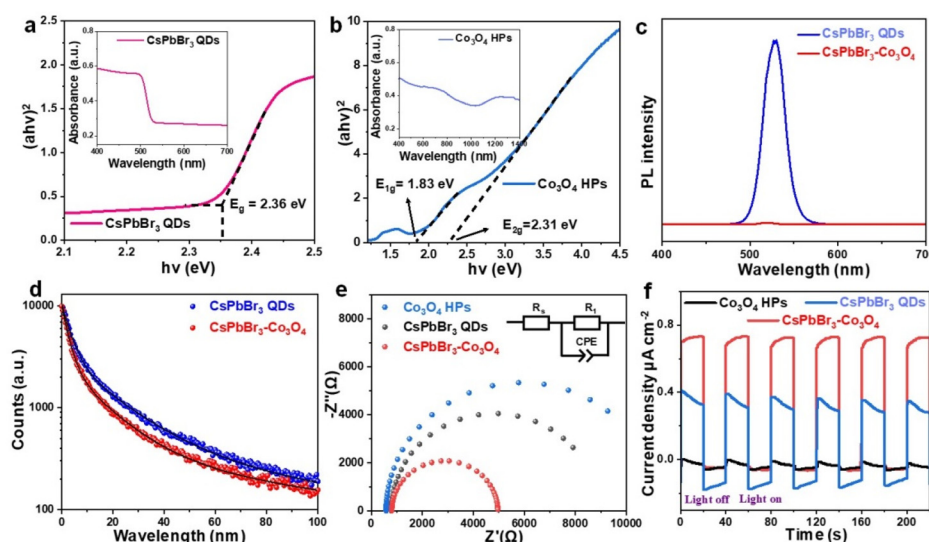


**Fig. 4** Tauc plots for energy bands and their corresponding insets depicting the diffuse reflectance spectra curves for (a)  $\text{CsPbBr}_3$  QDs and (b)  $\text{Co}_3\text{O}_4$  HPs. (c) Steady-state photoluminescence spectra, and (d) time-resolved photoluminescence spectroscopy of  $\text{CsPbBr}_3$  QDs and the  $\text{CsPbBr}_3$ – $\text{Co}_3\text{O}_4$  heterojunction. (e) Electrochemical impedance spectra and (f) transient photocurrent spectra of all the as-prepared products.

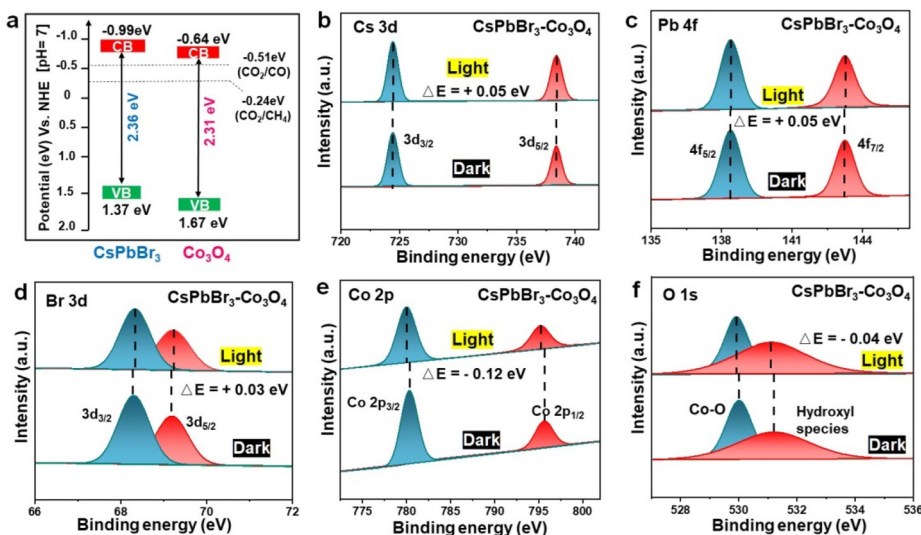


**Fig. 5** (a) Redox potentials and band alignment of the  $\text{CsPbBr}_3\text{-Co}_3\text{O}_4$  heterojunction. The *in situ* XPS analysis of (b) Cs 3d, (c) Pb 4f, (d) Br 3d, (e) Co 2p, and (f) O 1s, showing the electron-rich and electron-deficient sides in the  $\text{CsPbBr}_3\text{-Co}_3\text{O}_4$  heterojunction.

and  $\text{Co}_3\text{O}_4$  HPs (Fig. 4e). The markedly inhibited resistance in  $\text{CsPbBr}_3\text{-Co}_3\text{O}_4$  would promote charge transfer. Likewise, the  $\text{CsPbBr}_3\text{-Co}_3\text{O}_4$  shows the highest photocurrent with high repeatability (Fig. 4f). This result further supports the accelerated separation of  $\text{e}^-\text{-h}^+$  pairs as well as highlights that an accessible route builds up (*i.e.*, heterointerface) by decorating  $\text{CsPbBr}_3$  QDs on  $\text{Co}_3\text{O}_4$  HPs.

### 3.4. Uncovering charge redistribution on the intimately coupled heterointerface and the corresponding catalytic mechanism

To further shed light on the interfacial charge-carrier flux, and their transfer route, particularly the accumulation of reductive electrons, the *in situ* XPS spectra were conducted under dark and visible light irradiation, respectively. As can be seen, the binding energies corresponding to Cs 3d, Pb 4f, and Br 3d exclusively underwent a positive shift (Fig. 5a-c) under light, which demonstrates a decrease of the electron density in the  $\text{CsPbBr}_3$  side. In the meantime, the peak attributed to Co 2p and O 1s shifted to lower binding energy, suggesting an increased electron density at the  $\text{Co}_3\text{O}_4$  side (Fig. 5e and f). Such patterns verify the continuous transfer of photoinduced electrons from  $\text{CsPbBr}_3$  to  $\text{Co}_3\text{O}_4$ . In other words,  $\text{Co}_3\text{O}_4$  plays a role as a supporting matrix to evoke and gather electrons from  $\text{CsPbBr}_3$  QDs, allowing electron localization on the active surface of  $\text{Co}_3\text{O}_4$ . At the same time, an uninterrupted separation of  $\text{e}^-\text{-h}^+$  pairs occurs in  $\text{CsPbBr}_3$  owing to the significantly improved light harvesting ability and abundant exposed surface. Therefore, the electron-rich and electron-deficient phenomena occur simultaneously to balance the electron redistribution in the  $\text{CsPbBr}_3\text{-Co}_3\text{O}_4$  heterojunction. Notably, except for the negative shift in O 1s spectra (Fig. 5f), no new peak belonging to OVs appeared, validating the structural permanence of  $\text{Co}_3\text{O}_4$  in the heterojunction.

Furthermore, the work function ( $\Phi$ ) is another pivotal factor for charge carrier kinetics, particularly at the heterointerfaces. The  $\Phi$  for  $\text{CsPbBr}_3$  QDs and  $\text{Co}_3\text{O}_4$  HPs are 4.39 eV and 5.74 eV respectively.<sup>33,52</sup> So, a larger  $\Phi$  value of  $\text{Co}_3\text{O}_4$  refers to its lower Fermi level ( $E_f$ ) than that of  $\text{CsPbBr}_3$ , implying that the flow of electrons is from  $\text{CsPbBr}_3$  to  $\text{Co}_3\text{O}_4$  which is consistent with the outcomes of *in situ* XPS. This would hasten the extraction of reductive electrons from  $\text{CsPbBr}_3$  to  $\text{Co}_3\text{O}_4$ , thus suppressing the recombination of  $\text{e}^-\text{-h}^+$  pairs. In a word,  $\text{CsPbBr}_3$  facilitated the rapid and continuous electron transfer *via* shorter diffusion pathways due to the size effect, and  $\text{Co}_3\text{O}_4$  spontaneously accepted the electrons and accumulated on its active surface to exclusively participate in  $\text{CO}_2$  reduction under the irradiation of solar light.

Based on the above results, the proposed  $\text{CO}_2$  photoreduction mechanism over the  $\text{CsPbBr}_3\text{-Co}_3\text{O}_4$  hybrid has been described. As illustrated in Fig. 6a,  $\text{CsPbBr}_3$  and  $\text{Co}_3\text{O}_4$  in the heterojunction have a staggered band alignment (type-II). In addition, the  $\text{CsPbBr}_3\text{-Co}_3\text{O}_4$  heterojunction holds enough

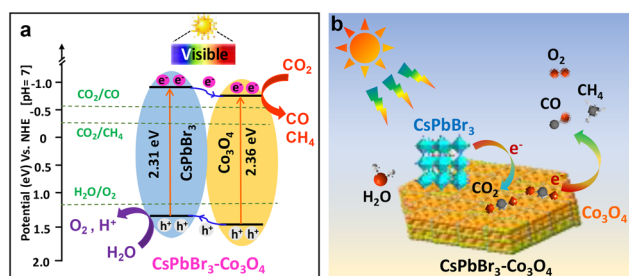


**Fig. 6** (a) Photoexcited charge separation and their transfer route over the  $\text{CsPbBr}_3\text{-Co}_3\text{O}_4$  heterojunction under visible light irradiation. (b) Schematic diagram depicting the continuous flow of electrons from  $\text{CsPbBr}_3$  towards  $\text{Co}_3\text{O}_4$  enabling the photocatalytic conversion of  $\text{CO}_2$ .

negative CB and positive VB potentials to reduce  $\text{CO}_2$  and oxidize water, respectively. Under light irradiation, electrons and holes can be generated in both  $\text{CsPbBr}_3$  and  $\text{Co}_3\text{O}_4$ . Subsequently, the photoinduced electrons are transferred from CB of  $\text{CsPbBr}_3$  to CB of  $\text{CO}_3\text{O}_4$  (Fig. 6b), causing electron localization at the  $\text{CO}_3\text{O}_4$  side, making it suitable to conduct the  $\text{CO}_2$  reduction reaction (as mentioned earlier in the *in situ* XPS analysis section). In the meantime, holes are transported in opposite directions *i.e.*, from VB of  $\text{CO}_3\text{O}_4$  to VB of  $\text{CsPbBr}_3$ , building a hole-rich  $\text{CsPbBr}_3$  side, favourable for oxidizing  $\text{H}_2\text{O}$  to  $\text{O}_2$  and  $\text{H}^+$ . Accordingly, the breaking of  $\text{C}=\text{O}$  bonds in  $\text{CO}_2$  occurred at the electron-rich  $\text{Co}_3\text{O}_4$  side, where the coupling of electron and protons took place, for instance,  $2\text{e}^-$  and  $8\text{e}^-$  get coupled with  $2\text{H}^+$  and  $8\text{H}^+$  to produce  $\text{CO}$  and  $\text{CH}_4$ , respectively, as presented in eqn (1) and (2). Thus, the effective charge separation enables the uninterrupted electron–proton integrative reaction to realize highly efficient  $\text{CO}_2$  photocatalytic reduction over the  $\text{CsPbBr}_3$ – $\text{Co}_3\text{O}_4$  heterojunction.



## 4. Conclusions

In conclusion, a facile solution-processed room-temperature method was developed to fabricate a new  $\text{CsPbBr}_3$ – $\text{Co}_3\text{O}_4$  heterojunction photocatalyst for visible-light-driven  $\text{CO}_2$  conversion. The successful formation of the  $\text{CsPbBr}_3$ – $\text{Co}_3\text{O}_4$  hybrid was confirmed by XRD, TEM, HRTEM and XPS analysis. The enhanced generation of  $\text{CO}$  ( $35.40 \mu\text{mol g}^{-1} \text{h}^{-1}$ ) and  $\text{CH}_4$  ( $29.2 \mu\text{mol g}^{-1} \text{h}^{-1}$ ) with a high  $R_{\text{electron}}$  rate ( $304.4 \mu\text{mol g}^{-1} \text{h}^{-1}$ ) was realized on the  $\text{CsPbBr}_3$ – $\text{Co}_3\text{O}_4$  hybrid, which outperformed the counter products and some state-of-the-art photocatalysts. The formation of staggered band alignment and an intimately contacted heterointerface led to robust separation and directional transfer of charge carriers. Because of the uninterrupted flow of reductive  $\text{e}^-$ , an electron enrichment zone was obtained at the active site of  $\text{Co}_3\text{O}_4$ , which ensured the efficient conversion of  $\text{CO}_2$ . This work describes the potential of designing a new perovskite-based heterojunction that could enable efficient charge separation to achieve better solar-driven  $\text{CO}_2$  conversion.

## Author contributions

Xin Zhong: methodology, investigation, data curation, and writing the original draft. Xinmeng Liang: methodology, investigation, data curation, and writing the original draft. Xinyu Lin: methodology, investigation, and validation. Malik Zeeshan Shahid: writing the original draft, visualization, investigation, and data curation. Jin Wang: supervision, conceptualization, descriptions, and funding acquisition. Zhengquan Li: supervision, conceptualization, descriptions, and funding acquisition.

## Conflicts of interest

There are no conflicts to declare.

## Acknowledgements

This work was financially supported by the National Natural Science Foundation of China (21701143, 21975223), the Natural Science Foundation of Zhejiang Province (LGG19B010002, LZ22B030002), and the Industrial Key Projects of Jinhua City (2021A22383).

## References

- 1 J. Wang, Y. Shi, Y. Wang and Z. Li, Rational design of metal halide perovskite nanocrystals for photocatalytic  $\text{CO}_2$  reduction: Recent advances, challenges, and prospects, *ACS Energy Lett.*, 2022, **7**, 2043–2059.
- 2 S. Yin, X. Zhao, E. Jiang, Y. Yan, P. Zhou and P. Huo, Boosting water decomposition by sulfur vacancies for efficient  $\text{CO}_2$  photoreduction, *Energy Environ. Sci.*, 2022, **15**, 1556–1562.
- 3 Y. Feng, C. Wang, P. Cui, C. Li, B. Zhang, L. Gan, S. Zhang, X. Zhang, X. Zhou, Z. Sun, K. Wang, Y. Duan, H. Li, K. Zhou, H. Huang, A. Li, C. Zhuang, L. Wang, Z. Zhang and X. Han, Ultrahigh photocatalytic  $\text{CO}_2$  reduction efficiency and selectivity manipulation by single-tungsten-atom oxide at the atomic step of  $\text{TiO}_2$ , *Adv. Mater.*, 2022, **34**, 2109074.
- 4 J. Wang, L. Xiong, Y. Bai, Z. J. Chen, Q. Zheng, Y. Y. Shi, C. Zhang, G. C. Jiang and Z. Q. Li, Mn-doped perovskite nanocrystals for photocatalytic  $\text{CO}_2$  reduction: Insight into the role of the charge carriers with prolonged lifetime, *Sol. RRL*, 2022, **6**, 2200294.
- 5 S. Xu, Q. Shen, J. Zheng, Z. Wang, X. Pan, N. Yang and G. Zhao, Advances in biomimetic photoelectrocatalytic reduction of carbon dioxide, *Adv. Sci.*, 2022, 2203941.
- 6 S. H. Teo, C. H. Ng, Y. H. Ng, A. Islam, S. Hayase and Y. H. Taufiq-Yap, Resolve deep-rooted challenges of halide perovskite for sustainable energy development and environmental remediation, *Nano Energy*, 2022, **99**, 107401.
- 7 E. Gong, S. Ali, C. B. Hiragond, H. S. Kim, N. S. Powar, D. Kim, H. Kim and S.-I. In, Solar fuels: research and development strategies to accelerate photocatalytic  $\text{CO}_2$  conversion into hydrocarbon fuels, *Energy Environ. Sci.*, 2022, **15**, 880–937.
- 8 Y. Wang, E. Chen and J. Tang, Insight on reaction pathways of photocatalytic  $\text{CO}_2$  conversion, *ACS Catal.*, 2022, **12**, 7300–7316.
- 9 Ž. Kovačić, B. Likozar and M. Huš, Photocatalytic  $\text{CO}_2$  reduction: A review of Ab initio mechanism, kinetics, and multiscale modeling simulations, *ACS Catal.*, 2020, **10**, 14984–15007.

10 H. Bian, D. Li, S. Wang, J. Yan and S. F. Liu, 2D-C<sub>3</sub>N<sub>4</sub> encapsulated perovskite nanocrystals for efficient photo-assisted thermocatalytic CO<sub>2</sub> reduction, *Chem. Sci.*, 2022, **13**, 1335–1341.

11 S. D. Yang, H. Y. Li, H. M. Li, H. M. Li, W. S. Qi, Q. Zhang, J. Zhu, P. Zhao and L. Chen, Rational design of 3D carbon nitrides assemblies with tunable nano-building blocks for efficient visible-light photocatalytic CO<sub>2</sub> conversion, *Appl. Catal., B*, 2022, **316**, 121612.

12 M. Gao, J. Zhang, P. Zhu, X. Liu and Z. Zheng, Unveiling the origin of alkali metal promotion in CO<sub>2</sub> methanation over Ru/ZrO<sub>2</sub>, *Appl. Catal., B*, 2022, **314**, 121476.

13 L. Collado, P. Reñones, J. Fermoso, F. Fresno, L. Garrido, V. Pérez-Dieste, C. Escudero, M. D. Hernández-Alonso, J. M. Coronado, D. P. Serrano and V. A. D. O'Shea, The role of the surface acidic/basic centers and redox sites on TiO<sub>2</sub> in the photocatalytic CO<sub>2</sub> reduction, *Appl. Catal., B*, 2022, **303**, 120931.

14 S. Wei, Q. Heng, Y. Wu, W. Chen, X. Li and W. Shangguan, Improved photocatalytic CO<sub>2</sub> conversion efficiency on Ag loaded porous Ta<sub>2</sub>O<sub>5</sub>, *Appl. Surf. Sci.*, 2021, **563**, 150273.

15 X. Lin, S. Xia, L. Zhang, Y. Zhang, S. Sun, Y. Chen, S. Chen, B. Ding, J. Yu and J. Yan, Fabrication of flexible mesoporous black Nb<sub>2</sub>O<sub>5</sub> nanofiber films for visible-light-driven photocatalytic CO<sub>2</sub> Reduction into CH<sub>4</sub>, *Adv. Mater.*, 2022, **34**, 2200756.

16 J. Wang, S. Lin, N. Tian, T. Ma, Y. Zhang and H. Huang, Nanostructured metal sulfides: classification, modification strategy, and solar-driven CO<sub>2</sub> reduction application, *Adv. Funct. Mater.*, 2020, **31**, 2008008.

17 C. I. Ezugwu, S. Liu, C. Li, S. Zhuiykov, S. Roy and F. Verpoort, Engineering metal-organic frameworks for efficient photocatalytic conversion of CO<sub>2</sub> into solar fuels, *Coord. Chem. Rev.*, 2022, **450**, 214245.

18 C. B. Hiragond, N. S. Powar, J. Lee and S. I. In, Single-atom catalysts (SACs) for photocatalytic CO<sub>2</sub> reduction with H<sub>2</sub>O: activity, product selectivity, stability, and surface chemistry, *Small*, 2022, **18**, 2201428.

19 X. J. Liu, T. Q. Chen, Y. H. Xue, J. C. Fan, S. L. Shen, M. S. A. A. Hossain, M. A. Amin, L. K. Pan, X. T. Xu and Y. Yamauchi, Nanoarchitectonics of MXene/semiconductor heterojunctions toward artificial photosynthesis via photocatalytic CO<sub>2</sub> reduction, *Coord. Chem. Rev.*, 2022, **459**, 214440.

20 S.-H. Wang, F. Khurshid, P.-Z. Chen, Y.-R. Lai, C.-W. Cai, P.-W. Chung, M. Hayashi, R.-J. Jeng, S.-P. Rwei and L. Wang, Solution-processable naphthalene diimide-based conjugated polymers as organocatalysts for photocatalytic CO<sub>2</sub> reaction with extremely stable catalytic activity for over 330 hours, *Chem. Mater.*, 2022, **34**, 4955–4963.

21 S. Chen, H. Yin, P. Liu, Y. Wang and H. Zhao, Stabilisation and performance enhancement strategies for halide perovskite photocatalysts, *Adv. Mater.*, 2022, **35**, 2203836.

22 H. Huang, D. Verhaeghe, B. Weng, B. Ghosh, H. Zhang, J. Hofkens, J. A. Steele and M. B. J. Roeffaers, Metal halide perovskite based heterojunction photocatalysts, *Angew. Chem., Int. Ed.*, 2022, **61**, e202203261.

23 S. Purohit, K. L. Yadav and S. Satapathi, Metal halide perovskite heterojunction for photocatalytic hydrogen generation: progress and future opportunities, *Adv. Mater. Interfaces*, 2022, **9**, 2200058.

24 L. Y. Wu, Y. F. Mu, X. X. Guo, W. Zhang, Z. M. Zhang, M. Zhang and T. B. Lu, Encapsulating perovskite quantum dots in iron-based metal-organic frameworks (MOFs) for efficient photocatalytic CO<sub>2</sub> reduction, *Angew. Chem., Int. Ed.*, 2019, **58**, 9491–9495.

25 X. Zhu, L. Ge, Y. Wang, M. Li, R. Zhang, M. Xu, Z. Zhao, W. Lv and R. Chen, Recent advances in enhancing and enriching the optical properties of Cl-based CsPbX<sub>3</sub> nanocrystals, *Adv. Opt. Mater.*, 2021, **9**, 2100058.

26 M. Ou, W. Tu, S. Yin, W. Xing, S. Wu, H. Wang, S. Wan, Q. Zhong and R. Xu, Amino-assisted anchoring of CsPbBr<sub>3</sub> perovskite quantum dots on porous g-C<sub>3</sub>N<sub>4</sub> for enhanced photocatalytic CO<sub>2</sub> reduction, *Angew. Chem., Int. Ed.*, 2018, **57**, 13570–13574.

27 M. Madi, M. Tahir and S. Tasleem, Advances in structural modification of perovskite semiconductors for visible light assisted photocatalytic CO<sub>2</sub> reduction to renewable solar fuels: A review, *J. Environ. Chem. Eng.*, 2021, **9**, 106264.

28 Y. F. Mu, W. Zhang, X. X. Guo, G. X. Dong, M. Zhang and T. B. Lu, Water-tolerant lead halide perovskite nanocrystals as efficient photocatalysts for visible-light-driven CO<sub>2</sub> reduction in pure water, *ChemSusChem*, 2019, **12**, 4769–4774.

29 L. Clinckemalie, D. Valli, M. B. J. Roeffaers, J. Hofkens, B. Pradhan and E. Debroye, Challenges and opportunities for CsPbBr<sub>3</sub> perovskites in low- and high-energy radiation detection, *ACS Energy Lett.*, 2021, **6**, 1290–1314.

30 J. Wang, J. Liu, Z. Du and Z. Li, Recent advances in metal halide perovskite photocatalysts: Properties, synthesis and applications, *J. Energy Chem.*, 2021, **54**, 770–785.

31 G. Gao, Q. Xi, H. Zhou, Y. Zhao, C. Wu, L. Wang, P. Guo and J. Xu, Novel inorganic perovskite quantum dots for photocatalysis, *Nanoscale*, 2017, **9**, 12032–12038.

32 Q. A. Akkerman, T. P. T. Nguyen, S. C. Boehme, F. Montanarella, D. N. Dirin, P. Wechsler, F. Beiglbock, G. Raino, R. Erni, C. Katan, J. Even and M. V. Kovalenko, Controlling the nucleation and growth kinetics of lead halide perovskite quantum dots, *Science*, 2022, **377**, 1406–1412.

33 Z. Zhang, L. Li, Y. Jiang and J. Xu, Step-scheme photocatalyst of CsPbBr<sub>3</sub> quantum dots/BiOBr nanosheets for efficient CO<sub>2</sub> Photoreduction, *Inorg. Chem.*, 2022, **61**, 3351–3360.

34 X. Y. Yue, L. Cheng, J. J. Fan and Q. J. Xiang, 2D/2D BiVO<sub>4</sub>/CsPbBr<sub>3</sub> S-scheme heterojunction for photocatalytic CO<sub>2</sub> reduction: Insights into structure regulation and Fermi level modulation, *Appl. Catal., B*, 2022, **304**, 120979.

35 C. C. Lin, T. R. Liu, S. R. Lin, K. M. Boopathi, C. H. Chiang, W. Y. Tzeng, W. C. Chien, H. S. Hsu, C. W. Luo, H. Y. Tsai, H. A. Chen, P. C. Kuo, J. Shiue, J. W. Chiou, W. F. Pong,

C. C. Chen and C. W. Chen, Spin-polarized photocatalytic  $\text{CO}_2$  reduction of Mn-Doped perovskite nanoplates, *J. Am. Chem. Soc.*, 2022, **144**, 15718–15726.

36 Q. Wang, J. Wang, J. C. Wang, X. Hu, Y. Bai, X. Zhong and Z. Li, Coupling  $\text{CsPbBr}_3$  quantum dots with covalent triazine frameworks for visible-light-driven  $\text{CO}_2$  reduction, *ChemSusChem*, 2021, **14**, 1131–1139.

37 L. Ding, B. Borjigin, Y. Li, X. Yang, X. Wang and H. Li, Assembling an affinal 0D  $\text{CsPbBr}_3$ /2D  $\text{CsPb}_2\text{Br}_5$  architecture by synchronously in situ growing  $\text{CsPbBr}_3$  QDs and  $\text{CsPb}_2\text{Br}_5$  nanosheets: enhanced activity and reusability for photocatalytic  $\text{CO}_2$  reduction, *ACS Appl. Mater. Interfaces*, 2021, **13**, 51161–51173.

38 J. Wang, J. Wang, N. Li, X. Du, J. Ma, C. He and Z. Li, Direct Z-scheme 0D/2D heterojunction of  $\text{CsPbBr}_3$  quantum Dots/ $\text{Bi}_2\text{WO}_6$  nanosheets for efficient photocatalytic  $\text{CO}_2$  reduction, *ACS Appl. Mater. Interfaces*, 2020, **12**, 31477–31485.

39 Y. Jiang, H. Y. Chen, J. Y. Li, J. F. Liao, H. H. Zhang, X. D. Wang and D. B. Kuang, Z-Scheme 2D/2D heterojunction of  $\text{CsPbBr}_3$ / $\text{Bi}_2\text{WO}_6$  for improved photocatalytic  $\text{CO}_2$  reduction, *Adv. Funct. Mater.*, 2020, **30**, 2004293.

40 Z. J. Chen, Y. G. Hu, J. Wang, Q. Shen, Y. H. Zhang, C. Ding, Y. Bai, G. C. Jiang, Z. Q. Li and N. Gaponik, Boosting photocatalytic  $\text{CO}_2$  reduction on  $\text{CsPbBr}_3$  perovskite nanocrystals by immobilizing metal complexes, *Chem. Mater.*, 2020, **32**, 1517–1525.

41 S. Wan, M. Ou, Q. Zhong and X. Wang, Perovskite-type  $\text{CsPbBr}_3$  quantum dots/UiO-66( $\text{NH}_2$ ) nanojunction as efficient visible-light-driven photocatalyst for  $\text{CO}_2$  reduction, *Chem. Eng. J.*, 2019, **358**, 1287–1295.

42 Z.-C. Kong, J.-F. Liao, Y.-J. Dong, Y.-F. Xu, H.-Y. Chen, D.-B. Kuang and C.-Y. Su, Core@Shell  $\text{CsPbBr}_3$ @Zeolitic imidazolate framework nanocomposite for efficient photocatalytic  $\text{CO}_2$  reduction, *ACS Energy Lett.*, 2018, **3**, 2656–2662.

43 Y. F. Xu, M. Z. Yang, B. X. Chen, X. D. Wang, H. Y. Chen, D. B. Kuang and C. Y. Su, A  $\text{CsPbBr}_3$  perovskite quantum dot/Graphene oxide composite for photocatalytic  $\text{CO}_2$  reduction, *J. Am. Chem. Soc.*, 2017, **139**, 5660–5663.

44 Q. Zhang, P. Yang, H. Zhang, J. Zhao, H. Shi, Y. Huang and H. Yang, Oxygen vacancies in  $\text{Co}_3\text{O}_4$  promote  $\text{CO}_2$  photoreduction, *Appl. Catal., B*, 2022, **300**, 120729.

45 Z. Feng, X. Zhu, J. Yang, K. Zhong, Z. Jiang, Q. Yu, Y. Song, Y. Hua, H. Li and H. Xu, Inherent facet-dominant effect for cobalt oxide nanosheets to enhance photocatalytic  $\text{CO}_2$  reduction, *Appl. Surf. Sci.*, 2022, **578**, 151848.

46 P. Yang, Q. Zhang, Z. Yi, J. Wang and H. Yang, Rational electronic control of carbon dioxide reduction over cobalt oxide, *J. Catal.*, 2020, **387**, 119–128.

47 L. Huang, B. Li, B. Su, Z. Xiong, C. Zhang, Y. Hou, Z. Ding and S. Wang, Fabrication of hierarchical  $\text{Co}_3\text{O}_4$ @ $\text{CdIn}_2\text{S}_4$  p-n heterojunction photocatalysts for improved  $\text{CO}_2$  reduction with visible light, *J. Mater. Chem. A*, 2020, **8**, 7177–7183.

48 L. Wang, J. Wan, Y. Zhao, N. Yang and D. Wang, Hollow multi-shelled structures of  $\text{Co}_3\text{O}_4$  dodecahedron with unique crystal orientation for enhanced photocatalytic  $\text{CO}_2$  reduction, *J. Am. Chem. Soc.*, 2019, **141**, 2238–2241.

49 J. Y. Choi, C. K. Lim, B. Park, M. Kim, A. Jamal and H. Song, Surface activation of cobalt oxide nanoparticles for photocatalytic carbon dioxide reduction to methane, *J. Mater. Chem. A*, 2019, **7**, 15068–15072.

50 W. Chen, B. Han, C. Tian, X. Liu, S. Liang, H. Deng and Z. Lin, MOFs-derived ultrathin holey  $\text{Co}_3\text{O}_4$  nanosheets for enhanced visible light  $\text{CO}_2$  reduction, *Appl. Catal., B*, 2019, **244**, 996–1003.

51 X. Huang, Q. Shen, J. Liu, N. Yang and G. Zhao, A  $\text{CO}_2$  adsorption-enhanced semiconductor/metal-complex hybrid photoelectrocatalytic interface for efficient formate production, *Energy Environ. Sci.*, 2016, **9**, 3161–3171.

52 C. Gao, Q. Meng, K. Zhao, H. Yin, D. Wang, J. Guo, S. Zhao, L. Chang, M. He, Q. Li, H. Zhao, X. Huang, Y. Gao and Z. Tang,  $\text{Co}_3\text{O}_4$  Hexagonal platelets with controllable facets enabling highly efficient visible-light photocatalytic reduction of  $\text{CO}_2$ , *Adv. Mater.*, 2016, **28**, 6485–6490.

53 L. Wang, J. Deng, Z. Lou and T. Zhang, Nanoparticles-assembled  $\text{Co}_3\text{O}_4$  nanorods p-type nanomaterials: One-pot synthesis and toluene-sensing properties, *Sens. Actuators, B*, 2014, **201**, 1–6.

54 L. Li, C. Zhang, R. Zhang, X. Gao, S. He, M. Liu, X. Li and W. Chen, 2D ultrathin  $\text{Co}_3\text{O}_4$  nanosheet array deposited on 3D carbon foam for enhanced ethanol gas sensing application, *Sens. Actuators, B*, 2017, **244**, 664–672.

55 A. Aljabour, H. Coskun, D. H. Apaydin, F. Ozel, A. W. Hassel, P. Stadler, N. S. Sariciftci and M. Kus, Nanofibrous cobalt oxide for electrocatalysis of  $\text{CO}_2$  reduction to carbon monoxide and formate in an acetonitrile-water electrolyte solution, *Appl. Catal., B*, 2018, **229**, 163–170.

56 Y. Gu, J. Ding, X. Tong, H. Yao, R. Yang and Q. Zhong, Photothermal catalyzed hydrogenation of carbon dioxide over porous nanosheet  $\text{Co}_3\text{O}_4$ , *J. CO<sub>2</sub> Util.*, 2022, **61**, 102003.

57 X. Zhu, H. Ji, J. Yi, J. Yang, X. She, P. Ding, L. Li, J. Deng, J. Qian, H. Xu and H. Li, A specifically exposed cobalt oxide/carbon nitride 2D heterostructure for carbon dioxide photoreduction, *Ind. Eng. Chem. Res.*, 2018, **57**, 17394–17400.

58 W. Yang, G. Ma, Y. Fu, K. Peng, H. Yang, X. Zhan, W. Yang, L. Wang and H. Hou, Rationally designed  $\text{Ti}_3\text{C}_2$  MXene@ $\text{TiO}_2$ / $\text{CuInS}_2$  Schottky/S-scheme integrated heterojunction for enhanced photocatalytic hydrogen evolution, *Chem. Eng. J.*, 2022, **429**, 132381.

59 X.-T. Liu, B.-H. Li, X.-J. Wang, Y.-L. Li, J. Zhao, Y.-P. Li and F.-T. Li, Enhanced schottky effect in the  $\text{Ni}_2\text{P}$  cocatalyst via work function up-shift induced by  $\text{MoO}_2$  for boosting photocatalytic hydrogen evolution, *ACS Sustainable Chem. Eng.*, 2022, **10**, 10627–10640.

60 K. Liu, H. Zhang, T. Fu, L. Wang, R. Tang, Z. Tong and X. Huang, Construction of  $\text{BiOBr}/\text{Ti}_3\text{C}_2$ /exfoliated montmorillonite Schottky junction: New insights into exfoliated montmorillonite for inducing MXene oxygen functionali-

zation and enhancing photocatalytic activity, *Chem. Eng. J.*, 2022, **438**, 135609.

61 Y. Li, Q. Zhao, Y. Zhang, Y. Li, L. Fan, F.-T. Li and X. Li, In-situ construction of sequential heterostructured CoS/CdS/CuS for building “electron-welcome zone” to enhance solar-to-hydrogen conversion, *Appl. Catal., B*, 2022, **300**, 120763.

62 J. Li, L. Xu, T. Wang, J. Song, J. Chen, J. Xue, Y. Dong, B. Cai, Q. Shan, B. Han and H. Zeng, 50-Fold EQE Improvement up to 6.27% of solution-processed all-inorganic perovskite  $\text{CsPbBr}_3$  QLEDs via surface ligand density control, *Adv. Mater.*, 2017, **29**, 1603885.

63 N. Li, X. Chen, J. Wang, X. Liang, L. Ma, X. Jing, D. L. Chen and Z. Li, ZnSe Nanorods- $\text{CsSnCl}_3$  perovskite heterojunction composite for photocatalytic  $\text{CO}_2$  reduction, *ACS Nano*, 2022, **16**, 3332–3340.

64 D. Barreca, C. Massignan, S. Daolio, M. Fabrizio, C. Piccirillo, L. Armelao and E. Tondello, Composition and microstructure of cobalt oxide thin films obtained from a novel cobalt(II) precursor by chemical vapor deposition, *Chem. Mater.*, 2001, **13**, 588–593.

65 Z. Hu, L. Hao, F. Quan and R. Guo, Recent developments of  $\text{Co}_3\text{O}_4$ -based materials as catalysts for the oxygen evolution reaction, *Catal. Sci. Technol.*, 2022, **12**, 436–461.

66 Y. Xu, F. Zhang, T. Sheng, T. Ye, D. Yi, Y. Yang, S. Liu, X. Wang and J. Yao, Clarifying the controversial catalytic active sites of  $\text{Co}_3\text{O}_4$  for the oxygen evolution reaction, *J. Mater. Chem. A*, 2019, **7**, 23191–23198.

67 W. He, L. Liu, T. Ma, H. Han, J. Zhu, Y. Liu, Z. Fang, Z. Yang and K. Guo, Controllable morphology  $\text{CoFe}_2\text{O}_4$ / $\text{g-C}_3\text{N}_4$  p-n heterojunction photocatalysts with built-in electric field enhance photocatalytic performance, *Appl. Catal., B*, 2022, **306**, 121107.

68 S. Bai, J. Jiang, Q. Zhang and Y. Xiong, Steering charge kinetics in photocatalysis: intersection of materials syntheses, characterization techniques and theoretical simulations, *Chem. Soc. Rev.*, 2015, **44**, 2893–2939.